

The Seasonal Cycle of Significant Wave Height in the Ocean: Local vs Remote Forcing

Luke Colosi¹, Ana B. Villas Bôas¹, Sarah T. Gille¹

¹Scripps Institution of Oceanography, La Jolla, California

Key Points:

- Increases in significant wave height (SWH) during boreal and austral spring and summer months is present in most wind anomaly regions
- Magnitude of SWH increase is determined by local conditions within wind anomaly region
- Probability of swell decreases during wind anomaly events implying SWH increase occurs due to locally forced waves

Corresponding author: Sarah T. Gille, sgille@ucsd.edu

Corresponding author: Ana B. Villas Bôas, avillasb@ucsd.edu

12 **Abstract**

13 Significant wave height (SWH) provides insight about the interactions between the
 14 ocean and the atmosphere. In the Northern and Southern Hemispheres, wave heights have
 15 been observed to undergo an annual sinusoidal cycle in response to seasonal changes in
 16 storm patterns. In the California coast region, local expansion fan wind events lead to
 17 deviations in significant wave height during boreal spring and summer. Other coastal
 18 regions where supercritical channel flows occur due to coastal topography and atmospheric
 19 forcing during the early summer months include eastern boundary regions of ocean basins,
 20 the south Caribbean, and West Arabian Sea. Here, intraannual variability of surface grav-
 21 ity waves is analyzed globally in SWH and wind speed data, using over two decades of
 22 satellite-derived SWH and wind data. The location at which surface waves are gener-
 23 ated is used for validation of mechanisms driving wave characteristics. Phasing of the
 24 SWH seasonal cycle reveals that the primary hemisphere dominating the wave field has
 25 an abrupt and rough boundary through the equatorial region due in part to topography
 26 causing shadowing of waves. In summer wind anomaly (SWA) regions, the fraction of
 27 wave variability attributed to local wind events varies depending on local conditions. Global
 28 maps of probability of swell based on wave age confirm that wind anomaly regions typ-
 29 ically have locally forced waves during the spring and summer months.

30 **1 Introduction**

31 Surface gravity waves are fundamental to our understanding of the interactions be-
 32 tween the ocean and atmosphere, including the exchange of momentum, heat, gasses, and
 33 energy between the atmosphere and the ocean (Cavaleri et al., 2012). Gravity waves are
 34 commonly categorized by wave period and generation mechanism (Munk, 1951). In this
 35 study, we investigate ordinary surface waves, which are classified as having wave peri-
 36 ods between 1 to 30 seconds and being predominantly generated by wind. Over the past
 37 half century, remote sensing satellites have provided a global perspective on the large scale
 38 temporal and spatial variability of these waves. Present altimeters, radiometers, and scat-
 39 terometers are capable of repeatedly measuring wind speed and significant wave height
 40 (SWH) globally with spatial resolution on the order of 100km along swath or altimeter
 41 track.

42 Surface waves are generated by the wind and can propagate long distances across
 43 the oceans (Snodgrass et al., 1966). Due to the seasonality of storm systems which gen-
 44 erate remotely forced waves, SWH varies seasonally, and is expected to have higher val-
 45 ues in winter and lower values in summer months. Thus, the long-term temporal vari-
 46 ability of SWH is expected to be marked by a sinusoidal cycle with approximate period
 47 of 365 days which is referred to as the seasonal or annual cycle. For example, Echevarria,
 48 Hemer, and Holbrook (2019) applied a principal component analysis approach to a global
 49 wind wave hindcast developed by the Centre for Australian Weather and Climate Re-
 50 search (CAWCR) and found that most of the variance in SWH was explained by sea-
 51 sonal cycle.

52 However, the wave field in many regions of the world oceans is strongly influenced
 53 by other physical phenomena, such as climate modes and regional-scale wind variabil-
 54 ity which can result in deviations from the SWH seasonal cycle. Villas Bôas, Gille, Ma-
 55 zloff, and Cornuelle (2017) analyzed a distinct deviation occurring in the California coast
 56 region due to a local wind phenomena called expansion fan winds (EFWs) which forms
 57 due to atmospheric conditions and costal topography (Winant et al., 1988). This devi-
 58 ation is characterized as an increase or simply a bump in SWH during the spring and
 59 early summer months due to local EFW events generating locally forced waves that dom-
 60 inate the wave field (Villas Bôas et al., 2017).

This same supercritical channel flow has been hypothesized by Winant et al. (1988) to be present in other oceanic regions that have coastal topography and atmospheric conditions similar to California. These regions include the west coast of Australia, the coast of Namibia in southern Africa, the coast of Chile, the southern Caribbean sea, the northwest coast of Africa near Morocco, and in the Arabian sea near the tip of Somalia. These regions are a combination of eastern boundary current regions (EBRs), monsoon regions, and regions significantly sheltered from remotely forced waves. Hereon they will be referred collectively as summer wind anomaly (SWA) regions.

By analyzing intraannual variability of SWH for surface gravity waves and wind speed (WSP) on a global scale from 1993 to 2015 using satellite remote sensing, we investigate SWA regions to determine if the same seasonal cycle deviation as in the California Coastal region is present and if a corresponding maximum in wind speed seasonal cycle is correlated to the SWH deviation. In addition, the structural distribution of the parameters of the annual and semi-annual cycle on a global scale is explored in order to give insight into the general forcing mechanisms and parameters of the wave field influencing these deviations in SWH. In order to justify that SWH during the spring months in these SWA regions are locally forced, wave age can be used for separating growing seas from fully developed seas for collocated WSP and SWH data. We assess SWA regions in order to understand remote versus local forcing effects on the dominate characteristics of the wave field. This can lead to a deeper understanding of the wave climate and sea-state in these partially wind-sea dominated regions and aids in improving model representations of the wave field and gives possible expectations for prevailing sea-state dependent air-sea fluxes (Boas et al., 2019). Practical applications involve coastal shipping and navigation within SWA regions.

This paper is organized as follows. Section 2 explains the data sets used to conduct the time series analysis of global SWH data and the limitations of our analysis. Section 3 explores the general parameters of the annual and semi-annual SWH and WSP models for the entire time series globally as well as regional climatologies in order to demonstrate the relationship between the deviations from the seasonal cycle and the maximum in the WSP seasonal cycle. Section 4 uses wave age in order to illustrate that SWH measurements during the spring and summer months within SWA regions are observing wave fields dominated by locally forced wave rather than remotely forced wave justifying the claim that local wind events are causing the deviation from the seasonal cycle. Section 5 summarizes conclusions.

2 Methods

2.1 Remotely sensed Data

Wave data used in this study are drawn from two decades of cross-calibrated satellite altimeter SWH measurements produced by the Institut français de recherche pour l'exploitation de la mer (Ifremer). Ifremer's along track cross calibrated SWH altimeter data was collected from multiple near pole non-sun synchronous satellites over the time period of 1 January 1993 to 31 December 2015 and validated against in situ buoy observations. Here, we binned the daily along track data onto a 1° by 1° spatial grid. Satellites contributing to the analysis include ERS-1&2, TOPEX-Poseidon, GEOSAT Follow-ON (GFO), Jason-1, Jason-2, ENVISAT, Cryosat and SARAL AltiKa (Croiz-Fillon, 2017).

Wind data for this study is from the Cross Calibrated Multi-Platform version 2 wind vector analysis data (CCMP2) produced by Remote Sensing Systems. CCMP2's data product is released on a 0.25° by 0.25° spatial grid with 6 hourly temporal resolution. For this analysis, we daily averaged CCMP2 winds on a 1° by 1° spatial grid in order to match the SWH data. The CCMP2 product incorporates measurements from active

scatterometers, passive radiometers, in situ buoys, and modelled wind velocity data (Atlas et al., 2011a). CCMP reports wind in zonal and meridional components (Atlas et al., 2011a), which are used to compute WSP.

The Ifremer SWH product is not co-located temporally with the CCMP2 wind product; typical time differences are on the order of 6 hours. For point-to-point analysis, this would present a major obstacle due to the fact that the sea state including wave height or SWH and atmospheric conditions including WSP are highly variable on time scales of minutes to hours, meaning that SWH and WSP can change significantly within a 6 hour period. Therefore, the WSP measurement at a given location could have no relation at all to a SWH measurement taken 6 hours later at the same location. The analysis done in this study focuses on monthly averaged SWH and WSP.

2.2 Annual and Semi-Annual Model and Regional Climatology Analysis

In order to analyze the annual and semi-annual variability of SWH and WSP, at each grid point, we least-squares fitted SWH and WSP with a five parameters including the mean with annual and semi-annual sinusoidal cycles: Here, T is the duration of the annual cycle (12 months), t is time, and x_n are coefficients for the SWH or WSP model. A linear trend within the SWH and wind speed time series was accounted for within our analysis by detrending the WSP and SWH monthly data before computing the model and its parameters. To inspect the magnitude of the linear trend in the data, the least square fit above with a sixth term accounting for a linear trend was fitted to the data. The coefficient for linear trend term were used to give a rudimentary magnitude and significance of the linear trend. Young, Zieger, and Babanin (2011) preformed a similar analysis on SWH and WSP data from multiple satellite altimeter missions calibrated and validated by Zieger, Vinoth, and Young (2009). By using a least square fit accounting for the mean, annual cycle and higher frequency oscillations, the magnitude of the linear trend may be approximated via the slope of the trend. However, this approximations may contain spurious results when noise is present (Young et al., 2011). Fig 1 displays globally the magnitude of the linear trend and illustrates that the magnitude is significantly smaller than than amplitudes of the annual and semi-annual signal as well as the variance of the data. The linear trend magnitudes are slightly less than reported by Young et al. (2011). Whether the linear trend is an unreal artifact of the cross calibrated multi-platform data sets or is physically authentic, we do not know. However, the linear trend is still removed for completeness.

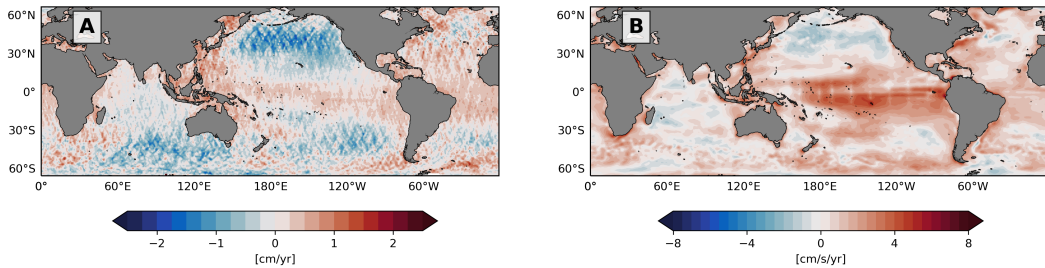


Figure 1. Magnitude of linear trend for monthly averaged (A) Ifremer SWH and (B) CCMP2 WSP.

In order to evaluate the goodness of fit of the model, the root mean square of the residual and coefficient of determination was used. The residual is defined as the difference between the model and the observed data. This method is a less robust method of

150 quantifying how well the model fits the observed data and is biased to have high residue
 151 in regions with high temporal variability.

$$\text{residual} = f(t) - \text{data} \quad (1)$$

152

$$\text{Root Mean Square Error} = \sqrt{\langle \text{residual}^2 \rangle} \quad (2)$$

153
 154
 155
 156

The coefficient of determination is the percent of variance of the data explained by the model and is calculated by taking the ratio of the summed squared error between each data point and the corresponding modelled data divided by the difference between the each data point and the mean value of the data.

$$r^2 = 1 - \frac{\sum_{i=0}^N \text{residue}}{\sum_{i=0}^N \text{total}} = 1 - \frac{\sum_{i=0}^N (y_i - f_i)^2}{\sum_{i=0}^N (y_i - \bar{y})^2} \quad (3)$$

157
 158

Here N is equivalent to the the number of observations. The coefficient of determination provides a more robust quantification of the goodness of fit of the model.

159
 160
 161

The parameters used to evaluate and compare the seasonal cycles spatially were the amplitude and phase constant. For the amplitude and phase constant of the annual and semi-annual cycle, these parameters were determined by the following equations:

$$\text{annual amplitude} = \sqrt{x_1^2 + x_2^2} \quad (4)$$

$$\text{semi - annual amplitude} = \sqrt{x_3^2 + x_4^2} \quad (5)$$

$$\text{annual phase} = \arctan\left(\frac{x_2}{x_1}\right) \quad (6)$$

$$\text{semi - annual phase} = \arctan\left(\frac{x_4}{x_3}\right) \quad (7)$$

(8)

162
 163
 164
 165
 166
 167
 168
 169
 170
 171
 172
 173
 174
 175
 176
 177
 178
 179

For the climatological analysis within SWA regions, SWH and WSP grid points within 4° by 4° square regions were first temporally averaged into single monthly averages and then spatially averaged. Therefore, we obtain SWH and WSP climatologies for the entire region in order to compare the SWH climatology with the WSP climatology to check for relationship between the SWH deviation and the WSP maximum. The 4° by 4° regions were picked by looking at seasonally averaged WSP maps within SWA regions. 4° by 4° regions that had anomalously high WSP and small spatial WSP gradients where chosen as seen in Fig 9 and Fig 10. For the northern hemisphere, the seasonal average from the boreal summer was used in order for the high WSP anomaly to be present in SWA regions. Likewise for the southern hemisphere, the seasonal average from the austral summer was used. Small spatial WSP gradient regions were favorable because the climatology analysis should be performed in regions with consistently high amplitude WSP maximum observations in order to have the highest likelihood of the wave field has significant influence by local winds. By spatially averaging over a regions including grid points with high and low amplitude maxima, our averaging would include two domains with very different time variability which would lead to having piece-wise rough climatologies. In addition, decently sized regions to spatially average data were used to bring down some of the noise present in SWA regions.

180
 181
 182

Seasonal progression maps of the first two statistical moments for Ifremer SWH and CCMP2 WSP data are computed in order to gain insight into the seasonal evolution and variability of the data (Fig 3.1 and Fig 3.1).

183 **2.3 Limitations of Data**

184 The data used in this study have limitations associated with retrieval methods and
 185 with multi-satellite intercalibration in order to obtain a continuous or “gap free” tem-
 186 poral or spatial data set for SWH and WSP.

187 As discussed, IFREMER SWH data set are cross calibrated between multiple satel-
 188 lite missions. However, in order to compile SWH over several satellite missions for cli-
 189 matological analysis, the data must be validated and verified that the data is homoge-
 190 neous (Queffeulou, 2004). IFREMER SWH data product has been validated by Queffeulou
 191 (2004) by comparing SWH measurements with in situ buoy observations for each satel-
 192 lite mission as well as ensured near homogeneity of SWH measurements between satel-
 193 lite missions. For WSP, CCMP2 cross calibration and assimilated surface wind data from
 194 satellite remote sensing scatterometers and microwave radiometers from multiple satel-
 195 lite missions use the variation analysis method (VAM) and European Centre for Medium-
 196 Range Weather Forecasts (ECMWF) modelled surface winds to validate this product and
 197 calibrate it with in situ buoy observations (Atlas et al., 2011b). Therefore, this assim-
 198 ilated and validated gridded product results in high spatial and temporal accuracy suit-
 199 able for climate studies (Atlas et al., 2011a). However, the CCMP2 WSP data set has
 200 a few caveats including having spurious trend due to assimilation process of modelled
 201 ECMWF data and underestimation of wind speeds in high wind regions due to modelled
 202 ECMWF winds tendency to underestimate wind speed (Atlas et al., 2011a). Fortunately,
 203 the annual and semi-annual cycles are stronger signals present in the WSP climate in
 204 SWA regions and would therefore not be considered a spurious trend. However, under-
 205 estimation of WSP could have effects on the analysis of SWA regions when the wind anomaly
 206 occurs.

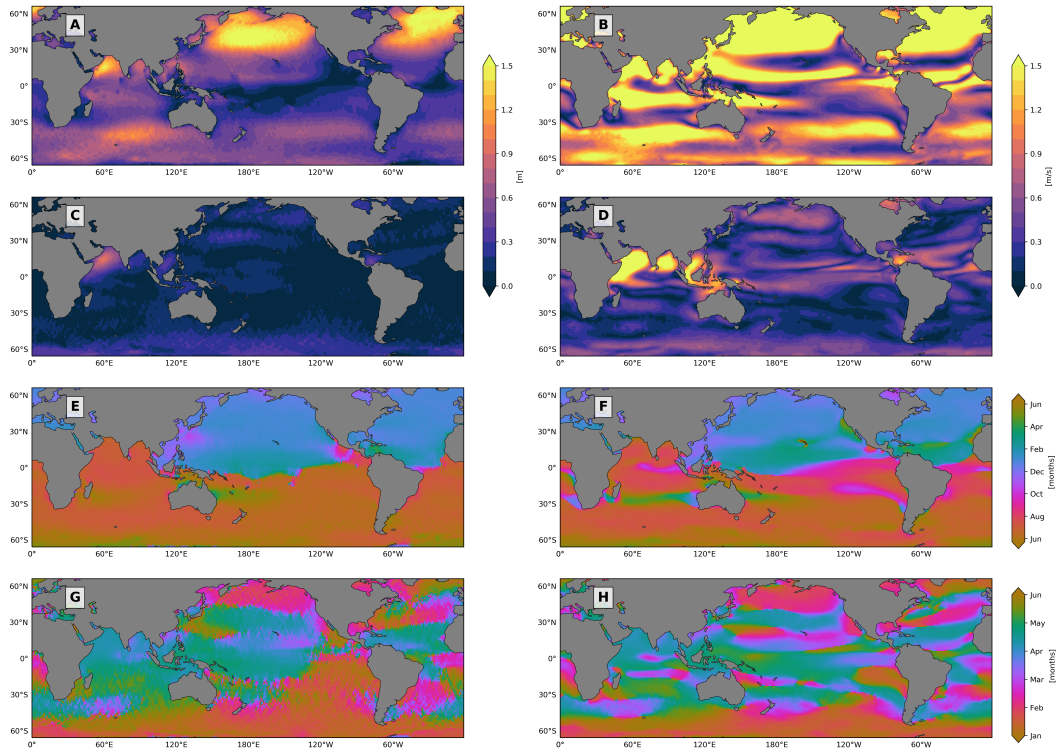
207 In addition, satellite altimetry data in near coastal region on the scales of 10km
 208 to 100km should be neglected from the analysis due to the spatial extent of the swath
 209 of the satellite. The footprint of satellite altimeter is on the order of 10km and averag-
 210 ing occurs over along track distances of 100km in order to increase the precision and ac-
 211 curacy of observations (Chelton et al., 2001). This means that the data can be slightly
 212 contaminated by the land in regions less than 10km off shore. Fortunately, the local wind
 213 anomalies persist for several hundreds of kilometer off shore allowing reliable SWH and
 214 WSP data satellite data to be recorded (Winant et al., 1988).

215 This study only focuses on time series analysis of integral or averaged parameter
 216 SWH instead of analyzing the wave spectrum. Other integral parameters that can be
 217 currently be obtained from satellites such as CFOSAT include peak frequency (or pe-
 218 riod) and mean wave direction however only a short temporal record exists (Boas et al.,
 219 2019). At any given point on earth, integral parameters describe only the dominant wave
 220 height, frequency, period, and direction of waves within the wave spectrum that is as-
 221 sociated with the highest spectral energy or elevation variance (Ardhuin, 2018). There-
 222 fore, weaker but still prevalent signals from swell and wind-sea waves are suppressed in
 223 the result as a result of this analysis. Echevarria et al. (2019) highlight this shortcom-
 224 ing of integral parameters in wave climatology analysis and present a climatological anal-
 225 ysis of multimodal directional wave spectrum via principal component analysis of the
 226 spectral data from Wave Watch 3 ECMWF reanalysis data. Semedo, Sušelj, Rutgers-
 227 son, and Sterl (2011) also used Wave Watch 3 ECMWF reanalysis data in order to an-
 228alyze the global wave climate. Integral parameters are used in this analysis with the un-
 229 derstanding of its limited ability to full describe all modes present in the wave spectrum.
 230 This study’s results only reflect the analysis of dominant highest spectral energy signal
 231 present.

232 3 SWH and WSP Intraannual Variability Analysis

233 3.1 Global parameters of Annual and Semi-annual Model and Implications 234 to SWA Regions

235 Figure 2 compares the Ifremer SWH annual and semi-annual cycle amplitude and
236 phase with CCMP2 WSP results. Notice that the phase has been converted from radi-
237 ans to months



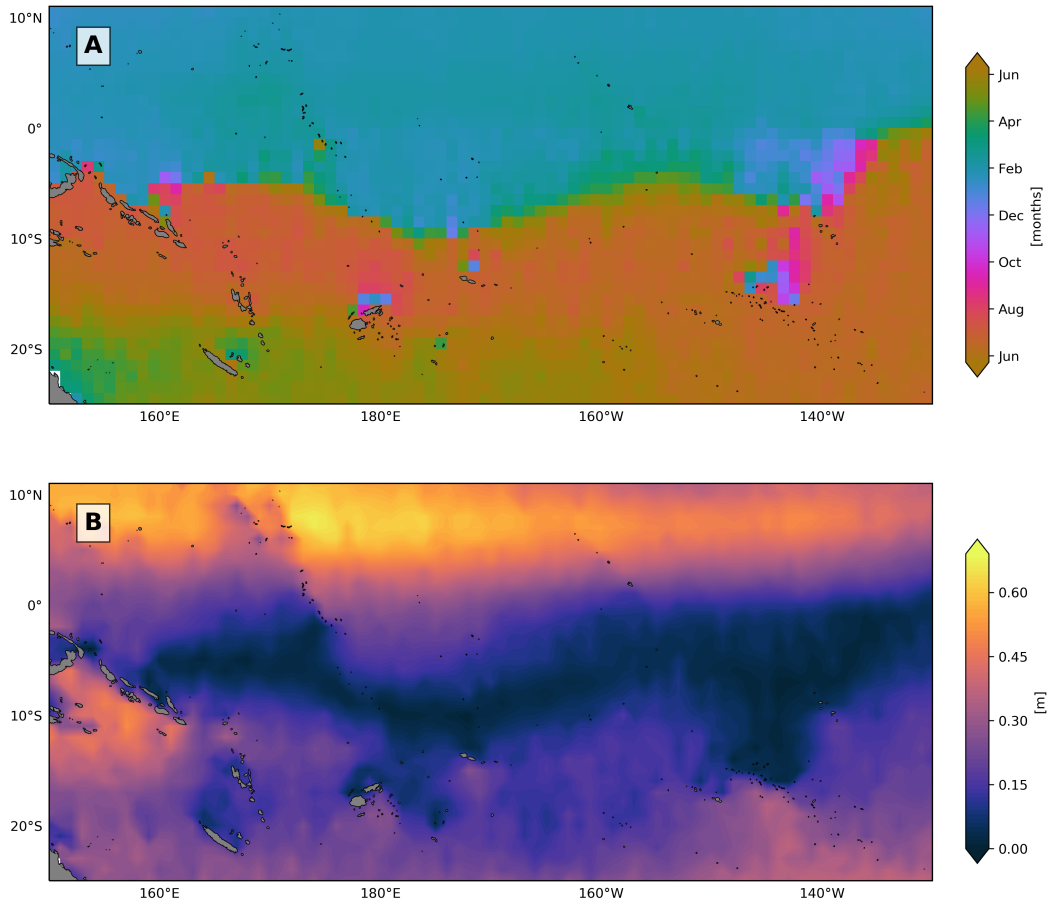
238 **Figure 2.** Amplitude of annual cycle for (A) Ifremer SWH and (B) CCMP2 WSP; amplitude
239 of semi-annual cycle for (C) Ifremer SWH and (D) CCMP2 WSP; phase of annual cycle for (E)
240 Ifremer SWH and (F) CCMP2 WSP; phase of semi-annual cycle for (G) Ifremer SWH and (H)
241 CCMP2 WSP. See text for details of computation.

242 The annual cycle phase map for SWH (Fig. 2E) shows that the phase of the sea-
243 sonal cycle in the Northern Hemisphere is approximately 6 months out of phase with the
244 Southern Hemisphere, with the timing of maximum wave height well aligned with the
245 timing of maximum WSP seasonal cycle (Fig. 2F). WSP is a common characteristic of
246 synoptic high latitude storm systems in the northern and southern hemisphere and ex-
247 periences a seasonal cycle (Fig. 6). Remotely forced waves generated from these near sur-
248 face winds will propagate away from these storm systems throughout ocean basins and
249 will predominately dominate the wave field (Semedo et al., 2011). This causes SWH of
250 these remotely forced waves to undergo a similar seasonal cycle (Fig. 4). Therefore, this
251 6-month phase shift illustrates that storm systems' annual frequency and intensity cy-
252 cles in the mid to high latitudes of the Northern and Southern Hemispheres set the sea-
253 sonal cycle of SWH. However in some regions where local wind events input a significant
254 amount of energy into the ocean, the SWH may become dominated by locally forced waves.

Other features in the SWH annual cycle phase map include higher spatial variability in the Southern Hemisphere than in the Northern Hemisphere, potentially due to the nontrivial wind systems present in the Southern Hemisphere experiencing high amplitude intraannual variability. The intraannual variability of storm system would directly effect the wave climate because remote and local storms or prevailing winds are one of the main forcing mechanisms generating these wind waves. Therefore, high spatial variability in phase exists in the southern hemisphere. In the equatorial region, the dominant phase changes roughly along a line where the amplitude of the seasonal cycle tends towards zero (Fig 2A). This boundary designates the transition from the seasonal cycle being primarily set by storm system originating in the Northern hemisphere to being primarily set by storm systems originating in the Southern Hemisphere. This smooth transition is expected in the region where the amplitude tends towards zero. This phase boundary in the Pacific and Atlantic is also known as a swell front (Young, 1999) and is the boundary between domains of dominance of swell from each hemisphere and discussed in Semedo et al. (2011) and Jiang and Chen (2013). However, waves propagating from the Northern and Southern Hemispheres coexist superimposed on the wave field at and beyond the swell front (Echevarria et al., 2019). This means that the waves will continue propagating in their respective directions into the opposite hemisphere.

In the tropical Pacific, several abrupt shifts in phase exist between 10° and 20° south at approximately 180°E and 145°W (Figure 3). One explanation for these abrupt phase shifts is island shadowing. Waves from the Southern Ocean propagating northward encounter the topography of Polynesian islands and break and dissipate on the shores facing the direction of the oncoming waves. The opposite side of the island does not encounter any of these remotely or locally forced waves. Therefore, the southern facing sides of these islands are in phase with the Southern Hemisphere seasonal cycle while the northern facing sides of the islands are in phase with the northern hemisphere because they are only exposed to southward traveling waves originating in the Northern Hemisphere. Some waves are able to refract between these islands as well. Waves from the Southern Ocean that are able to propagate through the Polynesian islands continue into the northern Pacific. Evidence for this northward propagation can be seen in a tongue of slightly higher phase constant value between the two indentations present on the phase boundary at approximately 175°E and 140°E (Figure 3A). Higher phase constant value refers to the maximum of the SWH annual cycle occurs during the spring months of May or April as it shifts towards the boreal winter.

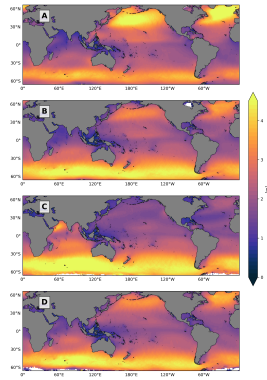
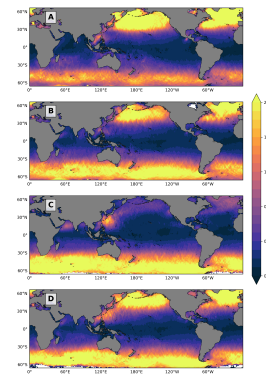
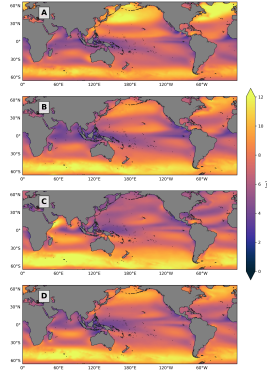
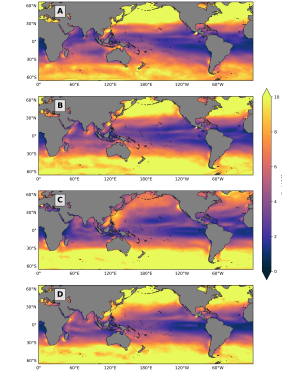
The phase transition from the Northern Hemisphere dominated domain to the Southern Hemisphere dominated domain occurs slightly south of the equator between 5° and 10°S in the west pacific staring at 170°W , and it slowly shifts equatorward while moving east across the Pacific (Figure 3A). Explanations for the geographic location of the boundary are linked to where the amplitude of the seasonal cycle tends to zero (Figure 3B). Other explanations include the following. Waves would encounter westward flowing south equatorial current (SEC), south equatorial countercurrent (SECC), the westward north equatorial current (NEC), or the north equatorial countercurrent (NECC). The SEC and SECC are located on average closest to the phase boundary, and they are known to be present between 5° and 10°S (Talley, 2011). However, the wave-current interactions between waves propagating into this region from the Northern and Southern Hemisphere have no effects of wave propagation when the velocities of the two are orthogonal. In addition, the wave-current interaction is on small scales and would be undetectable in satellite altimeter SWH data when the footprint of the satellite covers several kilometers of sea surface. Additionally, the phase boundary of the annual cycle does not line up with the intertropical convergence zone (ITCZ) characterized as a low pressure system with heavy precipitation and deep convection (Schneider et al., 2014) that causes very calm sea surface conditions. These calm sea surface conditions could be thought of as being associated with the low amplitude seasonal cycle region. However, low amplitude does not imply low SWH values because there is a mean value that offsets the SWH seasonal



289 **Figure 3.** (A) Ifremer SWH Annual cycle phase map in Polynesian island region illustrating
 290 island shadowing, (B) Ifremer SWH annual cycle amplitude map in Polynesian island region

311 oscillations from zero. By looking at the SWH seasonal mean (Fig 4), the mean is rel-
 312 atively low, but not the minimum value of the equatorial region. In addition, the intertrop-
 313 ical convergence zone annual migrates between 9°N in boreal summer and 2°N in bo-
 314 real winter in the central Pacific following the warmer hemisphere (Schneider et al., 2014).
 315 This is significantly far from the phase boundary. Wave to wave interactions and non-
 316 conservative forcing could possible play a significant role here; however, the angle between
 317 each wave's group velocity determines significantly how energy and momentum will be
 318 distributed throughout the system. By looking at fig 3, we see that islands within this
 319 region play a significant role in setting the shape of the minimum annual cycle ampli-
 320 tude region for SWH. Islands outline the near zero contour for amplitude and therefore
 321 significantly affect how waves propagate into this region and how those waves will in-
 322 teract with each other.

323 Other interesting structures exist in near coastal regions and in the Atlantic in Fig. 2E.
 324 In the Atlantic, there is also a smooth phase boundary transition with one abrupt phase
 325 shift close to the western side of the Atlantic. On the western side, the phase boundary
 326 is almost vertical following a line of constant latitude. This dynamic boundary also oc-
 327 curs in the zero amplitude SWH seasonal cycle region and is slightly below the equator.
 328 In addition, just off the coast of Mexico, there is an out of phase region that is close to
 329 the near zero amplitude region. These other structures will be left for further research.

330 **Figure 4.** Ifremer SWH Seasonal Mean**Figure 5.** Ifremer SWH Seasonal Variance332 **Figure 6.** CCMP2 WSP Seasonal Mean**Figure 7.** CCMP2 WSP Seasonal Variance

334 The SWH and WSP annual cycle phase maps display an interesting relationship
 335 between deviations in the SWH seasonal cycle and local wind anomalies that are gen-
 336 erated by similar mechanics to expansion fan wind events off the California coast. In the
 337 SWH annual phase constant maps, deviations from the seasonal cycle predominantly can-
 338 not be observed in the cases when the deviation in the seasonal cycle is less than the max-
 339 imum values of the seasonal sinusoidal oscillations. However, this is not the case for all
 340 SWA regions, as will be explained later.

341 For the WSP annual cycle phase map (Fig. 2F), the phase constant clearly outlines
 342 regions where local wind anomalies similar to the EFW events off the coast of Califor-
 343 nia are present. The wind anomalies are characterized on the phase map by a π phase
 344 shift in the WSP seasonal cycle or a 6 month shift is the WSP seasonal cycle maximum
 345 from the surrounding region. By looking at the global map of phase for WSP, we observe
 346 that SWA regions typically are out of phase with their surrounding regions. For exam-
 347 ple, in the EBR off the coast of Australia (Fig 2F), the phase reveals that the maximum
 348 in the WSP seasonal cycle occurs during the austral summer within the SWA region. Out-
 349 side of the SWA region, WSP reaches a maximum during the austral winter.

350 The WSP phase map has structural similarities to the SWH phase map due to the
 351 proportional relationship between wind waves and the storm systems that generate them:
 352 the Northern and Southern Hemispheres are six months out of phase with each other,
 353 and the Southern Hemisphere has more spatial variability (Fig 2F). These intricate South-
 354 ern Hemisphere features are due to the dynamic intraannual variability of storm systems
 355 especially in the Indian ocean (Schott et al., 2009). However, there are many differences

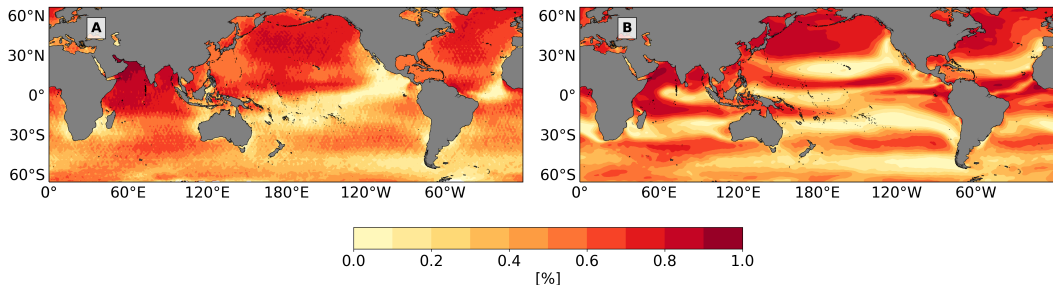
356 between SWH and WSP phase maps. The phase boundary in the Pacific designating the
 357 transition in the hemisphere that is primarily setting the WSP seasonal cycle is further
 358 north, and the majority of the boundary is smooth and continuous, without abrupt changes
 359 in phase on the eastern side of the Pacific, but with a slightly high gradient on the west
 360 side. In the Atlantic, the phase boundary is a smooth transition and is more linear in
 361 shape than the SWH phase boundary in the Atlantic. The phase boundary in the At-
 362 lantic follows closely the near zero WSP amplitude of the annual cycle; however, in the
 363 Pacific, the amplitude does not tend to zero near or at the equator. Furthermore, the
 364 Indian Ocean has prominent structures of swooping fingers of high phase constant val-
 365 ues which are again due to dynamics of intraannual variability of storm system and pre-
 366 vailing winds (Schott et al., 2009).

367 Coefficient of determination global maps can be used to assess the percentage of
 368 the variability explained by the model in order to understand whether there are other
 369 processes not accounted for by the annual and semi-annual cycles. Fig 8 shows that the
 370 percent of variability explained by the model is high in the North Pacific and Atlantic
 371 and low in the Southern Ocean for SWH and WSP. For SWH, the percent variation ex-
 372 plained reaches a minimum in the near-equatorial region in the Pacific and Atlantic. For
 373 WSP, the features of high percent variation explained are complex throughout the equa-
 374 torial region with varying amounts from near 100% to near 0%. These low values in the
 375 equatorial region may be attributed partly to the decadal oscillation of El Niño. The per-
 376 cent variation varies for each SWA region. For both SWH and WSP, SWA regions range
 377 from having 10% to 40% of the variation explained by the two modes represented in the
 378 model with the exception of the Arabian and Caribbean seas which have near 100% vari-
 379 ation explained. There are especially low values off the coast of Chile and Namibia for
 380 SWH and off the coasts of California, Chile, and North Africa for WSP. The Arabian
 381 and South Caribbean seas have higher percent variation explained by the model because
 382 these regions primarily have wave and wind forced by mechanics that have annual and
 383 semi-annual frequencies. In support of this argument, both of the coefficient of deter-
 384 minations geographic features follow very closely with features in the annual and semi-
 385 annual amplitude of SWH and WSP maps such that the percent of variation explained
 386 by the model is highest in regions with high amplitude and lowest in region of near zero
 387 amplitude. This means that the model explains the variability significantly less in most
 388 of the SWA regions because there are weak annual and semi-annual cycles. In addition,
 389 there are other forcing mechanism at work in these regions that contribute more signif-
 390 icantly to the wave and wind field. One of these forcing mechanisms for the wave field
 391 is the deviation from the seasonal cycle from local wind events. The goodness of fit quan-
 392 tified by the coefficient of determination should not be thought of as a test of reliabil-
 393 ity of the model. Rather, it is an indication of physical processes not accounted for by
 394 the model, which we want to explore to understand the underlying mechanisms gener-
 395 ating the variability in the wave and wind fields.

399 3.2 Regional Climatologies of SWA Regions

400 In order to obtain a closer look at the seasonal cycle within these SWA regions, cli-
 401 matologies or monthly mean SWH and WSP time series were computed from January
 402 1st, 1993 to December 31st, 2015 within 4° by 4° grid boxes. Fig 9 and Fig 10 show the
 403 regional climatologies from SWA regions in the Northern and Southern Hemispheres re-
 404 spectively as well as the 4° by 4° regions within each SWA regions where the climatol-
 405 ogy is computed. From these climatologies, a clear difference is seen between Northern
 406 and Southern Hemisphere SWA regions.

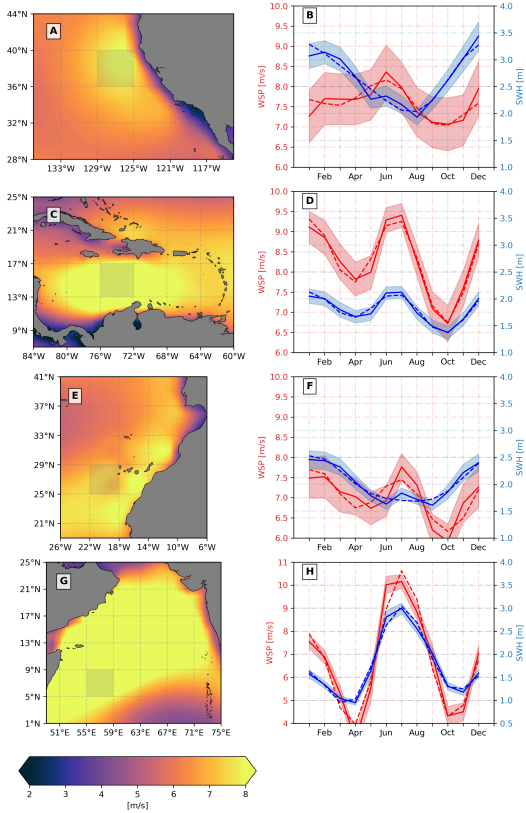
421 In all Northern Hemisphere SWA regions, the maximum in the WSP climatology
 422 occurs at the same time, when a deviation from the sinusoidal SWH seasonal cycle oc-
 423 curs. Examples include the Northern California and North African SWA regions (Fig 10B,F).
 424 Off the coast California, the WSP seasonal cycle reaches a maximum during the month



396 **Figure 8.** Global map of Coefficient of determination for Ifremer SWH (A) and CCMP2
 397 WSP (B) using Unweighted Annual and semi-annual Least Square Fit from January 1st, 1993 to
 398 December 31st, 2015 for a metric of the goodness of fit of the model.

425 of June. This peak is associated with an increase in SWH at the same time that the sea-
 426 sonal cycle is reaching a summer minimum. In the North African region off the coast of
 427 Morocco, a WSP maximum and a deviation from the SWH seasonal cycle are present
 428 in the month of July. In the Southern Hemisphere, the maximum in the WSP occurs dur-
 429 ing the austral summer in SWA regions, however there is only a small magnitude devi-
 430 ation from the SWH seasonal cycle occurring at the same time in the SWH climatology.
 431 Off the coast of western Australia (Fig 10B), a small magnitude deviation from the SWH
 432 annual cycle is present during the month of February when the maximum in the WSP
 433 climatology occurs. However, off the coast of Chile and Namibia (Fig 10D,F), deviations
 434 from the seasonal cycle are not present at all in the SWH climatology. Therefore, we pro-
 435 pose that Southern Hemisphere SWA regions' (Fig 10) local wind forcing have compar-
 436 atively less pronounced influence on the wave climate than in the Northern Hemisphere.
 437 This is presumed to occur because the magnitude of the deviation in the SWH cycle is
 438 determined by the local conditions and characteristics of the wave field within the re-
 439 gion. Local conditions refers to the exposure and distance of the SWA region from re-
 440 motely forced waves generation regions. In other words, how sheltered the SWA region
 441 is to regions with storms that produce high SWH remotely forced waves. By looking at
 442 looking at the two extreme cases of heavy sheltering and high exposure, the magnitude
 443 of the deviation from the SWH seasonal cycle can be explained.

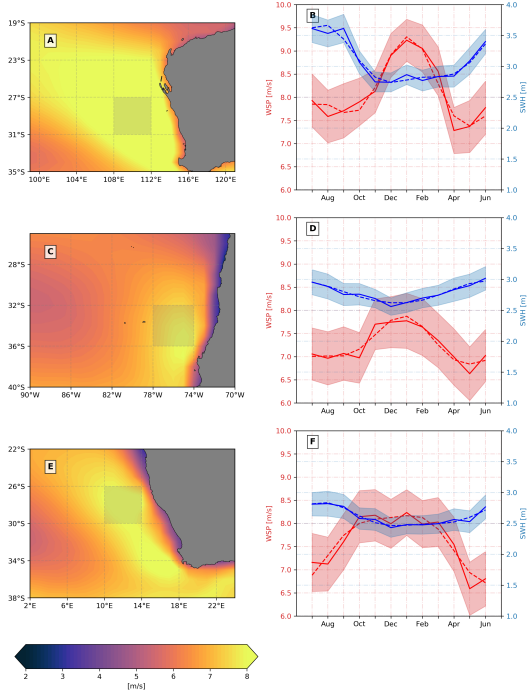
444 In the southern Caribbean Sea, the SWH climatology is in phase with the WSP
 445 climatology in Fig 9D. This implies that local wind events, including the wind anomaly
 446 during boreal summer and other wind events, predominately generate the waves within
 447 the region. This is due to the SWA region having little exposure to waves propagating
 448 from the high latitudes of the northern or southern Atlantic resulting in little of the wave
 449 energy being remotely forced. This sheltering from remotely forced waves is due to the
 450 Caribbean islands that ring the Caribbean sea (Fig 9C). The resulting seasonal variabil-
 451 ity, including the annual and semi-annual cycles, of this region is thus primarily set by
 452 local wind events within the Caribbean sea. Now by analyzing the increase in SWH oc-
 453 ccurring during the boreal summer due to the wind anomaly, the magnitude of this in-
 454 crease in SWH is relatively large such that the local maximum in SWH during the bo-
 455 real summer is of similar or equal magnitude to the local maximum of the annual cy-
 456 cle. Therefore, the local wind anomaly significantly alters the climatology of SWH be-
 457 cause the wave field tends to be dominated by locally forced wave for the majority of the
 458 year. This increase in SWH due to the wind anomaly also causing two maxima in SWH
 459 per year. This explains the near out of phase values seen in the Caribbean sea with re-
 460 spect to the rest of the Northern Hemisphere (Fig 2E). In addition, in Fig 2C,D, the large
 461 semi-annual cycle in the SWH and WSP semi-annual amplitude maps is clearly seen in
 462 the South Caribbean Sea due to the local wind anomaly. A similar semi-annual pattern



407 **Figure 9.** SWA regional maps of WSP averaged over the months of June, July, and August
 408 (left column) with Ifremer SWH (solid blue curve) and CCMP2 WSP (solid red curve) climatolo-
 409 gies in shaded 4° by 4° boxes within SWA regions located in the Northern Hemisphere. Shading
 410 in climatologies represents the standard error of the mean and dotted blue and red lines are the
 411 annual plus semi-annual cycle least-squares fitted to monthly climatology for SWH and WSP
 412 respectively. SWA regions include Northern California (A and B), Southern Caribbean Sea (C
 413 and D), North Africa near the coast of Morocco and western Sahara (E and F), North-Western
 414 Arabia Sea (G and H)

463 occurs in the Arabian and South China seas, where monsoon winds generate high locally
 464 forced waves. The Arabian Sea has a similar wave climate to the South Caribbean with
 465 the wave field having a high tendency to be dominated by locally forced waves, however,
 466 this SWA region is not sheltered from remotely forced waves that propagate up from the
 467 Southern Ocean. This examples the high magnitude increase in the SWH climatology
 468 during boreal summer (Fig 9H).

469 Off the coast of Western Australia, the increase in the SWH climatology during aus-
 470 tral summer has small magnitude due to this SWA region having high exposure to the
 471 Southern Ocean where larger storms produce larger SWH remotely forced waves. These
 472 waves propagating into the SWA region cause there to be a high mean SWH which the
 473 SWH seasonal cycle oscillates about. These remotely forced waves of large amplitude over-
 474 whelm the wave field within the SWA region and cause the locally forced waves to have
 475 significantly less affect such that locally forced waves are less likely to dominate the wave
 476 field from the remotely forced waves. Therefore, the remotely forced waves overwhelm
 477 the locally forced waves and tend to dominate the wave field for a significant majority
 478 year with a slight exception during January in the austral summer. During January, the



415 **Figure 10.** SWA regional maps of WSP averaged over the months of December, January, and
 416 February (left column) with Ifremer SWH (solid blue curve) and CCMP2 WSP (solid red curve)
 417 climatologies in shaded 4° by 4° boxes within SWA regions located in the Southern Hemisphere.
 418 Shading and dotted lines are as in Fig. 9. SWA regions include Western Australia (A and B),
 419 Central Western coast of South America near Chile (C and D), and South-Western Coast of
 420 Africa near Namibia (E and F)

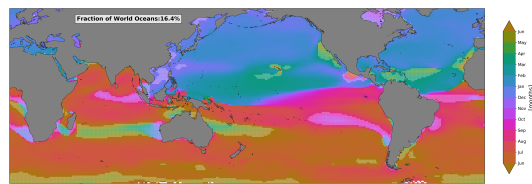
479 wave field tends to be dominated by locally forced waves and causes the slight increase
 480 in SWH. For the other two SWA regions in the Southern Hemisphere, the wave field is
 481 tends to be dominated by remotely forced waves all year round.

482 We conclude that the magnitude of the deviation in the SWH cycle is determined
 483 by the local conditions and characteristics of the wave field within the region. Conse-
 484 quentially, the magnitude of the deviation from the SWH seasonal cycle is less than North-
 485 ern Hemisphere SWA regions.

486 From each of these climatology of SWA regions (Fig 10, Fig 9), it is also observed
 487 that significance of the deviation varies from region to region. The significance of devi-
 488 ation from the seasonal cycle can be determined by considering the standard error of the
 489 mean (Figs. 9,10). In regions with high variance, the standard error of the mean is large
 490 enough that the deviation from the seasonal cycle is not statistically significant. This
 491 is seen in the west coast of Australia, coast of Chile, and the coast of Namibia.

492 To comprehend the global extent of anomalous local surface winds over the world
 493 oceans and their possible influences on the local wave field, the fraction of the world's
 494 oceans experiencing anomalous winds was computed using WSP annual cycle phase cal-
 495 culated from CCMP2 daily data. WSP phase is categorized as anomalous when the WSP
 496 phase is greater than $-\frac{\pi}{2}$ in the Northern Hemisphere corresponding to the maximum
 497 in WSP annual cycle occurring outside of boreal winter months and greater than $\frac{\pi}{2}$ and
 498 less than 0 in the Southern Hemisphere corresponding to the maximum in the WSP an-

499 nual cycle occurring outside of the Austral winter months. Observe that these wind anomalies
 500 are generated by a broad range of atmospheric forcings other than the expansion fan
 501 wind anomaly focused in this study. In order to compute this fraction, the world oceans
 502 were partitioned into southern and northern hemisphere basins including Indian Ocean,
 503 North and South Pacific, and North and South Atlantic Basins. Marginal Seas were mostly
 504 excluded as well as the equatorial regions across the Pacific and Atlantic oceans. We found
 505 that approximately 16.4% of the world oceans have anomalous high WSP during the spring,
 506 summer and fall months when it would be though to have lower WSP in the region. Fig 11
 507 shows geographically where these wind anomalies occur. This calculation is approximate
 508 and not highly rigorous, however it gives a general impression of the larger extend and
 509 the geographic locations where these wind anomalies occur. All SWA regions are con-
 510 sidered as anomalous except for the Arabian Sea. These regions categorized as having
 511 anomalous WSP phase may have a higher probability of the wave field being dominate
 512 by the local forced waves. However, this is depended on the local conditions of the wave
 513 field during the spring, summer, and fall months as discussed previously.



514 **Figure 11.** WSP annual cycle phase with gridded and lighter regions indicating anomalous
 515 wind regions

516 4 Wind-sea vs. Swell Dominance in SWA Regions

517 4.1 Local vs. Remotely Forced Waves

518 In order to evaluate whether SWA region waves are generated by local wind events
 519 or remote storms, we use wave age information to classify waves as locally or remotely
 520 forced. During a storm, wind blows over a length of ocean surface called fetch at cer-
 521 tain speed and for a given time duration, generating a packet of waves. Initially, waves
 522 that are formed by the wind are categorized as locally forced waves since the atmosphere
 523 is still supplying energy and momentum to the waves. These local forced waves are com-
 524 monly called wind-seas. The frequency or wavenumber spectrum is evolving as wave height,
 525 frequency, and period of the waves grow. These waves tend to have shorter periods (or
 526 high frequency and wavenumber) and thus travel at slower phase speeds than long pe-
 527 riod waves. Arduin, Chapron, and Collard (2009) observed swells propagating across
 528 ocean basins using satellite altimetry data from ENVISAT and showed that steep swell
 529 waves lose a significant fraction of there energy (up to 68%) over distances of 2800 km
 530 due to the laminar to turbulent transition in the air-side boundary layer. Wind-sea waves
 531 tend to be steep because of their short periods and high amplitudes, and this leads to
 532 significant dissipation over relatively short distances (Arduin et al., 2009). In addition,
 533 wind-sea wave dissipation could also be due to small scale wave-wave interactions, wave-
 534 current interactions and other atmospheric forcing. Therefore, the wind event must be
 535 relatively in close proximity to wind-sea waves. Once the wind is no longer inputting en-
 536 ergy and momentum into the waves, the waves are categorized as remotely forced waves.
 537 Remotely forced waves are commonly called fully developed seas or swell. In the case
 538 of swell waves, the wave field's frequency or wavenumber spectrum is set and is no longer
 539 evolving. These waves tend to have long periods (or low wave frequency and wavenum-
 540 ber) and have the ability to traverse long distances at higher phase speeds than short

541 period waves (Snodgrass et al., 1966). This leads to the dispersive nature of deep wa-
542 ter surface gravity waves (Snodgrass et al., 1966).

543 Waves measured by satellite altimeters represent a superposition of local wind waves
544 and remotely generated swell, and the altimeter does not distinguish frequency, period,
545 or direction. This is due to shape of the backscatter radiation off the sea surface received
546 by the satellite altimeter obtaining an average of the variability of the wave height present
547 in the satellites footprint (Chelton et al., 2001). Therefore, the SWH obtained from satel-
548 lite altimetry represents the wave height of the dominate waves within the wave field where
549 these waves may be generated locally or remotely. Globally, the wave field is consistently
550 dominated by swell (Chen et al., 2002; Semedo et al., 2011).

551 To distinguish between wind-sea and swell waves, wave age may be used. Wave age
552 quantifies the stage of development of waves and is therefore used to separate locally forced
553 waves from remotely forced waves through an empirically and theoretically determined
554 criterion (Alves et al., 2003). The wave age criterion is defined as

$$\text{Wave Age} = \frac{C_p}{U_{10}}, \quad (9)$$

555 where C_p is phase speed of the surface gravity wave or the speed of an individual wave
556 crest and U_{10} is the wind speed 10 meters above the ocean surface. The separation value
557 used in our analysis to distinguish locally and remotely forced waves is

$$\frac{C_p}{U_{10}} > 1.2 \quad \text{Remotely Forced Waves} \quad (10)$$

$$\frac{C_p}{U_{10}} \leq 1.2 \quad \text{Locally Forced Waves} \quad (11)$$

558 This criterion has been chosen and has empirically shown that wave growth stops or at
559 least becomes very slow when wave age is greater than 1.2 (Donelan et al., 1992). This
560 corresponds with waves crests travelling 20% faster than the wind speed 10 meters above
561 the ocean surface, so that the waves are outrunning the wind and not able to receive fur-
562 ther wind energy input. We assume that the satellite observes deep water waves, with
563 a wavelength much less than the water depth. For deep water waves, the deep water dis-
564 perssion relationship yields a peak phase speed:

$$C_p = \frac{g}{2\pi f_p} \quad (12)$$

565 4.2 Probability of Swell: Wave Age Method

566 Using wave age or other wind-sea and swell separation techniques, probability of
567 swell can be obtained to illustrated the amount of times the wave field is swell-dominated
568 for a given grid point as a fraction of the total amount of wave events which includes wind-
569 sea dominated and swell dominated events:

$$\text{Probability of swell} = \frac{N_{swell}}{N_{total}} \quad (13)$$

570 where N_{swell} is the number of time steps with wave age exceeding 1.2 representing a swell
571 dominated wave field and N_{total} is the total number of observations in the time series
572 .

573 Probability of Swell has been computed globally before by Jiang and Chen (2013)
574 and Semedo et al. (2011). Jiang and Chen (2013) used collocated satellite altimetry SWH
575 and radiometer WSP from the Jason-1 satellite mission to compute the probability of
576 swell using a wind-wave relationship derived from the Wave Modeling (WAM) Program
577 which was able to separate wind-seas from swell. Global seasonal maps of probability

of swell showed that the SWH observations by satellite altimetry are categorized primarily as remotely forced waves in all oceans with lower probability of swell in the Southern Ocean, in coastal regions, and along common storms tracks (Jiang & Chen, 2013). The probability of swell also undergoes a seasonal cycle with a decreasing seasonal cycle amplitude when approaching the equator. This decrease in probability of swell indicates an increase in the amount of wind events generating wind seas that dominate the wave field. Semedo et al. (2011) computed probability of swell using wave age as the separation criterion with European Centre for Medium-Range Weather Forecasts Re-Analysis (ERA-40) wave reanalysis. Semedo et al. (2011) found high probability of swell consistently throughout the world oceans implying that swell dominates the wave field (Semedo et al., 2011). Building on this analysis, wave energy spectra from ERA-40 was used separated into wind-sea and swell components using WAM separation frequencies and then SWH, mean wave period (MWP) and mean wave direction (MWD) were computed for each components. From seasonal maps of SWH decomposed into swell and wind sea components, the swell SWH was found to be always higher than the wind-sea component implying that swell dominates the wave spectra (Semedo et al., 2011).

By computing probability of swell globally for each season using wave age, probability of swell in SWA regions can confirm if the wave field observed during the spring months in SWA regions were dominated by wind-seas generated by the local wind anomaly or dominated by swell propagating from distant storms.

To calculate phase speed of waves and therefore wave age, we used Wave Watch 3 (WW3) modeled data with peak frequency. The Climate Forecast System Reanalysis (CFSR) winds provided the forcing to WW3 wave model in order to obtain the bulk parameters SWH and peak frequency with 6 hourly temporal and 0.5 degree spatial resolution. Wave age was computed after decreasing the spatial resolution of WW3 peak frequency and CFSR WSP to 1 degree and the temporal resolution to daily time steps. The WW3 and CFSR products were used instead of the coupled ECMWF wind product and WW3 wave parameters because CFSR WSP forcing WW3 SWH has more seasonal variability, and prediction accuracy improves in recent years (Stopa & Cheung, 2014). However, the WW3 and CFSR data sets has some potential biases, including overestimation of SWH and WSP as compared to in situ buoy observations and less temporal homogeneity than ECMWF forcing WW3 model which manifests itself as a slightly less smooth time series allowing CFSR and WW3 to more accurately model extreme weather events (Stopa & Cheung, 2014).

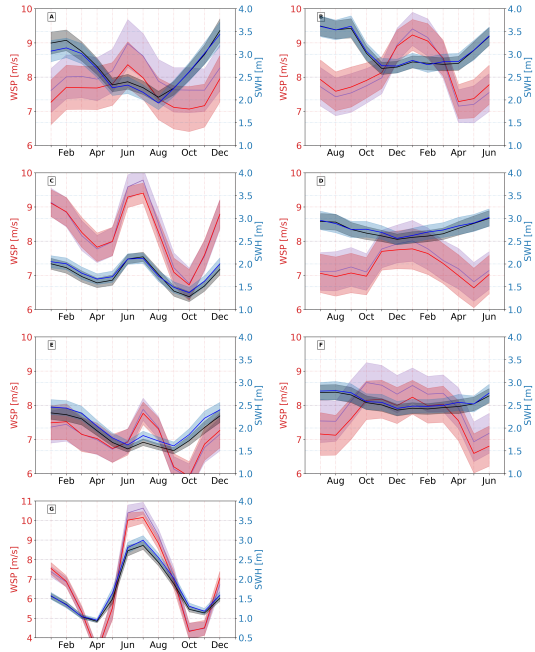
Before computing wave age with WW3 peak frequency using CFSR winds, we performed an elementary comparison test between remotely sensed SWH and WSP observations and WW3 SWH and CFSR WSP to understand how well the WW3 SWH and CFSR WSP were representing the observational data. This validation process included computing regional climatologies of WW3 SWH and CFSR WSP data in the same regions which that observational SWH and WSP climatologies were computed. In addition, the least-squares fit annual and semi-annual model was fitted to WW3 SWH and CFSR WSP and parameters of model were computed. Before performing comparison, the WW3 and CFSR data resolutions were decreased spatially to 1° by 1° and temporally to monthly time steps in order to match the data resolution of the least squares fit and regional climatology analysis. This prevents the model's small-scale spatial variability from artificially reducing correlations between the modelled and observed data. Regional climatologies of WW3 SWH and CFSR WSP data are compared to the Ifremer SWH and CCMP2 WSP in Fig 12, and the parameters of the least-squares fit of WW3 SWH and WSP (not shown). Both regional climatologies and parameters of the 5 parameter least square fit show high agreement in all of the SWA regions. This means that the amplitude and phase of the annual and semi-annual cycles agree well in SWA regions. However, there are small disparities present. For the regional climatologies, the model underestimates or agrees well with SWH in all SWA region climatologies except off the

631 California coast where the model consistently overestimates (Fig ??). The model over-
 632 estimates WSP off the coasts of California, Chile, and Namibia (Fig ??, Fig ??). In SWA
 633 regions off the coast of west Australia, north Africa, south Caribbean, and the Arabian
 634 Sea, the model overestimates the climatological maxima while underestimating the min-
 635 ima.

636 What are the consequences of overestimating or underestimating WSP on the prob-
 637 ability of swell if assuming peak frequency is unbiased and is held constant? By over-
 638 estimating WSP, wave age would decrease (increasing the denominator and decreases
 639 wave-age ratio) making it more likely for wave age drop below 1.2 and the wave field to
 640 be categorized as wind-sea dominated. This would lead to an decrease the probability
 641 of swell. Therefore, there may be a bias toward low probability of swell in SWA regions
 642 including Northern California, Chile, and Namibia. Using the same rational as before,
 643 for the southern Caribbean and Arabian Seas, there is a bias toward lower probability
 644 of swell during the boreal summer when the local wind anomaly occurs due to CFSR over-
 645 estimates WSP. For northern Africa, the probability of swell would have very little bias
 646 introduced by the WSP data due to the high accuracy of the model. For Western Aus-
 647 tralia, there is a slight bias toward lower probability of swell in the austral summer and
 648 higher probability of swell in the austral winter due to the CFSR underestimating WSP.
 649 Next, peak frequency must be validated by comparing it with in situ observations. Per-
 650 formance assessments of WW3 peak frequency have been studied in the Pacific basin by
 651 Hanson, Tracy, Tolman, and Scott (2009) using the Wave Model Evaluation and Diag-
 652 nostics System (WaveMEDS) to quantify the biases and overall performance scores for
 653 peak period for the entire wave field and for each component (wind-seas and swell) for
 654 the year 2000. The WW3 wave model had wind forcing from the high-quality, consis-
 655 tent, neutral stability wind fields NRAQ+ generated by the marine meteorology group
 656 at Oceanweather Inc. (Hanson et al., 2009). This is not the same wind forcing used to
 657 force the WW3 peak frequency data in this study, however, Hanson et al. (2009) has val-
 658 idated the peak frequency with realistic and reliable wind forcing. The WW3 modeled
 659 wave spectra is compared with wave spectra from seven deep-water buoy sites from the
 660 National Data Buoy Center (NDBC) and the Coastal Data Information Program (CDIP).
 661 Hanson et al. (2009) concluded that wave period agrees with in situ observations with
 662 a combined wind-sea and swell waves performance score of 0.93 for temporal correlations
 663 and 0.96 for quantile-quantile (Hanson et al., 2009).

664 The validation of the wave parameter peak frequency occurs with buoys located
 665 primarily in the Northern Hemisphere pacific. Other ocean basins have still yet to be
 666 rigorously validated for peak frequency. With the fore knowledge that the performance
 667 of peak frequency is unknown in other ocean basins, we use peak frequency based on the
 668 high accuracy of the model in representing in situ observations in the pacific.

673 Figure 13 is a seasonal progression global map of probability of swell which agrees
 674 very well with Semedo et al. (2011) global maps of probability of swell for DJF and JJA.
 675 As observed in Figure 13, SWA regions contained waves that were categorized as locally
 676 forced during the late spring and early summer months. This is illustrated by the prob-
 677 ability of swell being significantly lower in SWA regions than the surrounding areas around
 678 SWA regions during the season when the wind anomaly occurs. For the northern hemi-
 679 sphere, off the coast of California, the probability of swell significantly drops to 90% in
 680 the spring months and then below 75% in the summer months. Similarly, off the coast
 681 of North Africa, probability of swell drops to between 90% to 80% in the spring months
 682 and then below 75% in the summer months. Both the Caribbean and Arabian Seas are
 683 consistently below 75% through the entire year. This means that the wave field is more
 684 frequently dominated by locally forced waves than remotely forced waves. Therefore, this
 685 result agrees with the hypothesis that the deviation from the SWH annual cycle is a re-
 686 sult from locally forced waves dominating the wave field and causing a increase in SWH.
 687 For the Southern Hemisphere, the probability of swell in the SWA regions of West Aus-

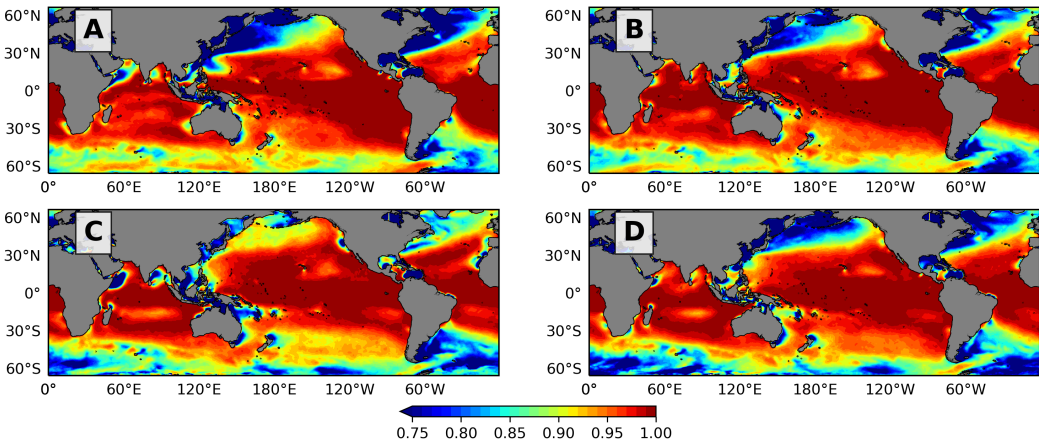


669 **Figure 12.** Northern Hemisphere SWA regions: (A) North California, (C) Southern
 670 Caribbean, (E) North Africa, and (G) Arabian Sea which are the same regions as in Fig 9 and
 671 Southern Hemisphere SWA regions: (B) West Australia, (D) coast of Chile, and (F) coast of
 672 Namibia which are the same regions as in Fig 10

688 tralia, Chile, and Namibia is not as low as in other SWA regions. This would also agree
 689 with the hypothesis that the SWA regions in the Southern Hemisphere have wave fields
 690 that are dominated predominately by remotely forced waves (and dominated by locally
 691 forced wave on fewer occurrences) due to their proximity to the Southern Ocean lead-
 692 ing to a less pronounced or nonexistent deviation from the SWH annual cycle.

696 5 Conclusion

697 This study has analyzed the seasonal cycles of SWH and WSP by least-squares fit-
 698 ting annual and semi-annual cycles to satellite observations. In most of the ocean SWH
 699 is higher in winter, indicating a response to high-latitude winter storms that generate
 700 equatorward-propagating swell. Exceptions occur in a few eastern boundary current re-
 701 gions and other wind anomaly regions, where strong local winds in spring or summer gen-
 702 erate wind waves that are out of phase with the winter storms. In the equatorial region,
 703 the boundary where the domains of dominance of Northern and Southern Hemisphere
 704 storm patterns setting the SWH annual cycle occurs off the equator in the Southern Hemis-
 705 pHERE following the line where the amplitude of the SWH annual cycle vanishes. This
 706 boundary is hypothesized to be influenced significantly by Polynesian islands affecting
 707 the way waves propagate through this region. Using regional climatology analysis in 4°
 708 by 4° boxes, we find that in SWA regions, the SWH can deviate from a sinusoidal an-
 709 nual cycle with winter maximum, instead indicating direct response to local winds. In
 710 SWA regions, the fraction of wave variability attributed to local wind events varies de-
 711 pending on local conditions. 16.4% of the world oceans including all but one of the SWA
 712 regions experience an anomalous WSP seasonal variability with the maximum of the WSP
 713 seasonal cycle occurring outside of the winter months of the respective hemisphere. The
 714 waves within each SWA region have low probability of swell during the spring and sum-



693 **Figure 13.** Seasonal progression of probability of swell using wave age criterion and WW3
 694 peak frequency and WSP from January 1st, 1993 to December 31st, 2015 where (A) DJF, (B)
 695 MAM, (C) JJA, and (D) SON

715 mer months of each hemisphere respectively. This implies that there is an increase in the
 716 number of times the wave field is dominated by wind-seas, supporting the hypothesis that
 717 the deviation from the SWH annual cycle results from wave that are locally forced by
 718 a local wind events.

719 Further research would include using spectral data from WW3 waves model forced
 720 by CFSR winds in order to separate wind-sea and swell parameters in SWA regions via
 721 spectral partitioning (Portilla et al., 2009) to further validate the claim that the devi-
 722 ation in the SWH seasonal cycle occurs from local wind events. In addition, local wind
 723 events should be further investigated to evaluate whether local winds result from the same
 724 atmospheric coastal topographic processes as in California.

725 By improving our understanding of the SWH climate globally with respect to the
 726 effects of local wind events, wave models can more accurately model and anticipate in-
 727 creases in SWH. Through understanding the wave climate in these SWA regions, we gain
 728 greater insight into determining at what times during the year remotely and locally forced
 729 wind waves dominate the wave field. Wave field's dominated by locally forced waves have
 730 strong interactions between waves and the lowest atmospheric layer (Cavaleri et al., 2012)
 731 due to the tendency of waves have short frequencies and steep. Processes involved in air-
 732 sea interactions that are amplifies by locally forced waves includes wave breaking and
 733 white capping. Both of these processes leads increase heat and mass fluxes from eject-
 734 ing sea spray including aerosols into the atmospheric boundary layer, injecting bubbles
 735 into the ocean, and causing waving-induced mixing in the upper ocean layer (Cavaleri
 736 et al., 2012). Sea-state dependent surface wave modulated fluxes of momentum, energy,
 737 heat and mass are all essential for climate models being able to close budgets to full de-
 738 scribe the coupled ocean-atmosphere system (Cavaleri et al., 2012). Understanding these
 739 fluxes begins with knowing the large scale temporally and spatially tendencies of the sea-
 740 state of the ocean. Through this study, identification of regions with high tendency for
 741 wind-sea dominated wave fields during the spring and summer months are established.
 742 From here, we can hypothesize general expectations for the significant air-interaction pro-
 743 cesses present in these regions.

744 **Acknowledgments**

745 This work was supported by NASA SWOT and Ocean Vector Winds Science Teams, Ana
 746 Villas Bôas Nasa fellowship, and the Hiestand Scholars program. The authors acknowl-
 747 edge Remote Sensing Systems for providing the multi-platform wind speed data avail-
 748 able from www.remss.com (<ftp://ftp.remss.com/ccmp/v02.0>) and the *French Research*
 749 *Institute for Exploitation of the Sea* (IFREMER) for providing the satellite altimetry sig-
 750 nificant wave height data (<ftp://ftp.ifremer.fr/ifremer/cersat/products/swath/altimeters/waves>)
 751 and WaveWatch 3 hindcast (<ftp://ftp.ifremer.fr/ifremer/ww3/HINDCAST>).

752 **References**

- 753 Alves, J. H. G., Banner, M. L., & Young, I. R. (2003). Revisiting the pierson-
 754 moskowitz asymptotic limits for fully developed wind waves. *Journal of physi-
 755 cal oceanography*, 33(7), 1301–1323.
- 756 Arduin, F. (2018). *Ocean waves in geosciences*. doi: 10.13140/RG.2.2.16019.78888/
 757 5
- 758 Arduin, F., Chapron, B., & Collard, F. (2009). Observation of swell dissipation
 759 across oceans. *Geophysical Research Letters*, 36(6).
- 760 Atlas, R., Hoffman, R. N., Ardizzone, J., Leidner, S. M., Jusem, J. C., Smith, D. K.,
 761 & Gombos, D. (2011a). A cross-calibrated, multiplatform ocean surface wind
 762 velocity product for meteorological and oceanographic applications. *Bull.
 763 Amer. Meteor. Soc.*, 92, 157–174. doi: 10.1175/2010BAMS2946.1
- 764 Atlas, R., Hoffman, R. N., Ardizzone, J., Leidner, S. M., Jusem, J. C., Smith, D. K.,
 765 & Gombos, D. (2011b). A cross-calibrated, multiplatform ocean surface wind
 766 velocity product for meteorological and oceanographic applications. *Bulletin of
 767 the American Meteorological Society*, 92(2), 157–174.
- 768 Boas, A. B. V., Arduin, F., Ayet, A., Bourassa, M. A., Brandt, P., Chapron, B., ...
 769 others (2019). Integrated observations of global surface winds, currents, and
 770 waves: Requirements and challenges for the next decade. *Frontiers in Marine
 771 Science*, 6.
- 772 Cavalieri, L., Fox-Kemper, B., & Hemer, M. (2012). Wind waves in the coupled cli-
 773 mate system. *Bulletin of the American Meteorological Society*, 93(11), 1651–
 774 1661.
- 775 Chelton, D. B., Ries, J. C., Haines, B. J., Fu, L.-L., & Callahan, P. S. (2001). Satel-
 776 lite altimetry. In *International geophysics* (Vol. 69, pp. 1–ii). Elsevier.
- 777 Chen, G., Chapron, B., Ezraty, R., & Vandemark, D. (2002). A global view of swell
 778 and wind sea climate in the ocean by satellite altimeter and scatterometer.
 779 *Journal of Atmospheric and Oceanic Technology*, 19(11), 1849–1859.
- 780 Croiz-Fillon, P. Q. . D. (2017). *Global altimeter swh data set* (Vol. 2; Tech. Rep.). ZI
 781 de la pointe du diable, CS10070, 29280 Plouzan, France.
- 782 Donelan, M., Skafel, M., Gruber, H., Liu, P., Schwab, D., & Venkatesh, S. (1992).
 783 On the growth rate of wind-generated waves. *Atmosphere-Ocean*, 30(3), 457–
 784 478.
- 785 Echevarria, E., Hemer, M., & Holbrook, N. (2019). Seasonal variability of the global
 786 spectral wind wave climate. *Journal of Geophysical Research: Oceans*, 124(4),
 787 2924–2939.
- 788 Hanson, J. L., Tracy, B. A., Tolman, H. L., & Scott, R. D. (2009). Pacific hind-
 789 cast performance of three numerical wave models. *Journal of Atmospheric and
 790 Oceanic Technology*, 26(8), 1614–1633.
- 791 Jiang, H., & Chen, G. (2013). A global view on the swell and wind sea climate by
 792 the jason-1 mission: a revisit. *Journal of Atmospheric and Oceanic Technology*,
 793 30(8), 1833–1841.
- 794 Munk, W. H. (1951). *Origin and generation of waves* (Tech. Rep.). SCRIPPS IN-
 795 STITUTION OF OCEANOGRAPHY LA JOLLA CALIF.

- 796 Portilla, J., Ocampo-Torres, F. J., & Monbaliu, J. (2009). Spectral partitioning and
797 identification of wind sea and swell. *Journal of atmospheric and oceanic tech-*
798 *nology*, 26(1), 107–122.
- 799 Queffeulou, P. (2004). Long-term validation of wave height measurements from al-
800 timeters. *Marine Geodesy*, 27(3-4), 495–510.
- 801 Schneider, T., Bischoff, T., & Haug, G. H. (2014). Migrations and dynamics of the
802 intertropical convergence zone. *Nature*, 513(7516), 45.
- 803 Schott, F. A., Xie, S.-P., & McCreary Jr, J. P. (2009). Indian ocean circulation and
804 climate variability. *Reviews of Geophysics*, 47(1).
- 805 Semedo, A., Sušelj, K., Rutgersson, A., & Sterl, A. (2011). A global view on the
806 wind sea and swell climate and variability from era-40. *Journal of Climate*,
807 24(5), 1461–1479.
- 808 Snodgrass, F., Hasselmann, K., Miller, G., Munk, W. H., & Powers, W. (1966).
809 Propagation of ocean swell across the pacific. *Philosophical Transactions of*
810 *the Royal Society of London. Series A, Mathematical and Physical Sciences*,
811 259(1103), 431–497.
- 812 Stopa, J. E., & Cheung, K. F. (2014). Intercomparison of wind and wave data from
813 the ecmwf reanalysis interim and the ncep climate forecast system reanalysis.
814 *Ocean Modelling*, 75, 65–83.
- 815 Talley, L. D. (2011). *Descriptive physical oceanography: an introduction*. Academic
816 press.
- 817 Villas Bôas, A. B., Gille, S. T., Mazloff, M. R., & Cornuelle, B. D. (2017). Char-
818 acterization of the deep water surface wave variability in the california current
819 region. *Journal of Geophysical Research: Oceans*, 122(11), 8753–8769.
- 820 Winant, C., Dorman, C., Friehe, C., & Beardsley, R. (1988). The marine layer off
821 northern california: An example of supercritical channel flow. *Journal of the*
822 *Atmospheric Sciences*, 45(23), 3588–3605.
- 823 Young, I. (1999). Seasonal variability of the global ocean wind and wave climate.
824 *International Journal of Climatology: A Journal of the Royal Meteorological*
825 *Society*, 19(9), 931–950.
- 826 Young, I., Zieger, S., & Babanin, A. V. (2011). Global trends in wind speed and
827 wave height. *Science*, 332(6028), 451–455.
- 828 Zieger, S., Vinoth, J., & Young, I. (2009). Joint calibration of multiplatform altimeter
829 measurements of wind speed and wave height over the past 20 years. *Jour-*
830 *nal of Atmospheric and Oceanic Technology*, 26(12), 2549–2564.